EFFECT OF TURBULENT WEDGES ON THE STEADY AND UNSTEADY AERODYNAMICS OF A FORWARD SWEPT LAMINAR WING

Michael Fehrs[1] and Christoph Kaiser[1]

[1]German Aerospace Center
Institute of Aeroelasticity
Bunsenstr. 10, 37073 Göttingen, Germany
michael.fehrs@dlr.de, christoph.kaiser@dlr.de

Keywords: correlation-based transition modeling, turbulent wedges, transition model validation, unsteady transonic flow

Abstract: Within the LuFo VI/2 project ULTIMATE, steady and unsteady wind tunnel tests in the European Transonic Windtunnel on a forward swept laminar wing configuration are conducted. The wind tunnel data are used to validate intermittency-based transition models in high Reynolds and transonic Mach number flows. This article presents a comparison of experimental data from the first steady wind tunnel campaign with coupled CFD-CSM computations. In the wind tunnel, turbulent wedges develop on the wing surface due to surface imperfections or surface contamination. Once these known turbulent wedges are included in the CFD-CSM simulation, a more precise computation of the aerodynamics of the wind tunnel model is possible. Additionally, the effect of the turbulent wedges on the unsteady aerodynamics is demonstrated for an unsteady pitching wing.

1 INTRODUCTION

In the LuFo VI/2 project ULTIMATE a forward swept laminar wing configuration is tested in the European Transonic Windtunnel (ETW) [1]. The application of laminar flow technology is a way to meet the ecological and economical constraints that demand the development of more efficient transport aircraft configurations by e.g. reducing the overall aircraft drag.

For the wind tunnel test campaign, a wing-fuselage half model named NLF-ECOWING-FSW is designed based on the TuLam short/medium range aircraft configuration [2]. The goal of the steady wind tunnel test is twofold: First, the performance of the overall wing/fuselage design will be assessed at realistic Mach and Reynolds numbers. Second, validation data for intermittency-based CFD transition prediction methods are provided. These data are needed for further validation of transition models at high Reynolds numbers as most experimental data used for calibration and validation are located in the low Reynolds number range. A consecutive unsteady wind tunnel test in a second wind tunnel campaign will provide data on unsteady boundary layer transition due to a pitch excitation of the wing.

The manufacturing/jig shape of the wing is developed based on previous coupled CFD-CSM computations [3]. A first set of computations with the TAU transition module [4,5] is performed by Helm et. al [6] based on the design shape of the wing. These computations show a large extent of laminar flow in agreement with the experimental wind tunnel data. Due to the high Reynolds number testing, turbulent wedges occur in the laminar boundary layer.

Helm et al. [7] show the effect of turbulent wedges on the aerodynamics of the CRM configuration in similar flow conditions based on the TAU transition module. In the present investigation, the DLR γ transition model is used [8] for transition prediction and a newly developed method is used to include turbulent wedges for intermittency-based transition models [9].

The next section will detail the experimental and numerical set-up. This includes a description of the solver including specific settings, the steady and unsteady coupling procedure, the finite element model, and CFD grids. The third section will present the numerical results in comparison to the experimental data and the preliminary unsteady investigation. The last section will conclude this article.

2 METHOD

2.1 NLF-ECOWING-FSW Configuration and Wind Tunnel Model

For the wind tunnel test in the ETW, a wing-fuselage half model is designed based on the TuLam short/medium range aircraft configuration [2]. It has a cruise Mach number of $M = 0.78$ (flight level $FL = 350$) with a design lift coefficient of $C_L = 0.52$. Figure 1 shows the NLF-ECOWING-FSW wind tunnel geometry. In the wind tunnel, the model is mounted on a peniche with a height of $0.04\,\mathrm{m}$, which is not included in the numerical investigations. The wind tunnel model has a half-span of $b/2 = 1.25\,\mathrm{m}$ and a reference chord of $c_{ref} = 0.28647\,\mathrm{m}$. The moment reference center of the wind tunnel model is located at the quarter chord location of the wing root at $(x, y, z) = (1.318881\,\mathrm{m},\ 0.0\,\mathrm{m},\ 0.0\,\mathrm{m})$. The model is made of maraging steel.
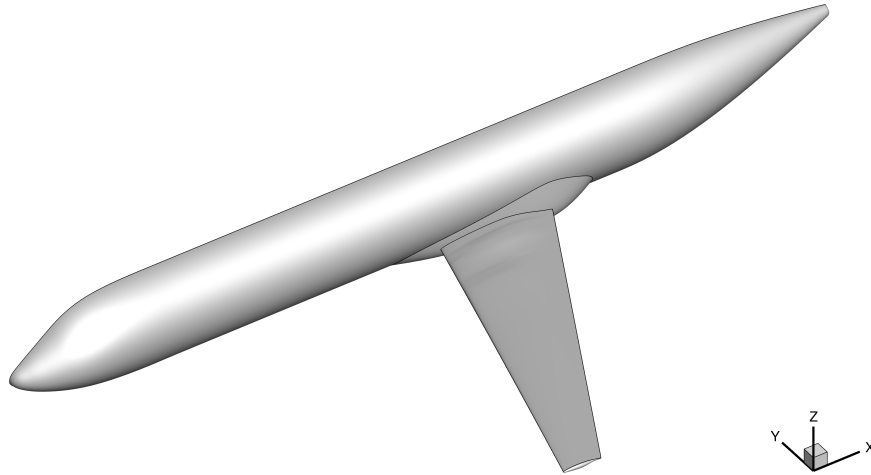

Figure 1: Jig shape geometry of the NLF-ECOWING-FSW wind tunnel model.

2.2 CFD Solver, Solver Settings, and CFD-CSM Methods

The DLR TAU-Code [10] is used in this investigation. The DLR γ transition model [8] is used in combination with the SST k-ω turbulence model [11] for transitional flows. Fully turbulent computations are based on the SST k-ω turbulence model. The SST k-ω turbulence model is augmented by employing the quadratic constitutive relation (QCR) [12] and the SST rotation correction (SSTRC) [13] for both types of flow.

A central scheme with artificial matrix dissipation [14] is used for the convective flux discretization of the mean flow equations in all computations. The convective fluxes of the turbulence equations are discretized with a second-order Roe upwind scheme. A local time step is used in

the steady computations in combination with an implicit Backward-Euler scheme to accelerate convergence employing an LU-SGS scheme [15]. A dual time stepping scheme [16] is used for the unsteady computations.

The coupled CFD-CSM computations are performed within the FlowSimulator [17] environment. For the static computations, Broyden's method [18] is used to iteratively obtain the static aeroelastic equilibrium based on modal coordinates. Therefore, in a pre-processing step, the mode shapes are interpolated to the nodes of the CFD surface grid by the thin plate spline method [19]. At each iteration, the aerodynamic forces are projected on these mode shapes and the modal displacements are found by the quasi-Newton step of Broyden's method. The modal displacements result in the deformation of the surface grid, which is propagated into the volume mesh by radial basis functions [20]. A total of 20 iterations is performed for each static coupling.

For the dynamic CFD-CSM computations, the coupled system represented in modal coordinates is integrated in the time domain by a staggered co-simulation, where deformations and aerodynamic forces are exchanged every time step. The unsteady modal displacements are obtained by the Newmark-beta method [21], which are then propagated into the CFD volume mesh like in the static scenario. Subsequently, the updated aerodynamic forces are computed and projected onto the modal coordinates. The pitch degree of freedom about the quarter chord line of the wing is considered by linearized displacements as only small pitch amplitudes are investigated.

Turbulent wedges are created by a numerical tripping given by a local increase in intermittency. The numerical transition tripping is based on the observation that intermittency-transport transition models are prone to react to small disturbances at high Reynolds numbers. A disturbance is defined based on a disturbance location Q and a disturbance radius δ_r. The intermittency at any point within the disturbance radius is set to $\gamma = 1$ to initiate the transition onset:

$$\gamma_w(\mathrm{Q}) = \begin{cases} 1, & \text{if } |\vec{r}| \leq \delta_r, \\ 0, & \text{if } |\vec{r}| > \delta_r, \end{cases} \tag{1}$$

$$\gamma = \min\left(\max\left(\gamma, \, \gamma_w\right), 1\right). \tag{2}$$

Grid points within the disturbance radius are identified in a pre-processing step and the γ_w field is kept for the whole solver run based on the grid point identification number. This allows to use mesh deformation without updating the coordinates of the disturbance during the computation.

Table 1: Parameters for Sutherland's law for N_2 [22]

parameter	value	unit
T_0	273	K
μ	$1.663 \cdot 10^{-5}$	N·s/m^2
S	107	K

The ETW uses nitrogen and an appropriate gas model needs to be used in the CFD-CSM computation to obtain the stagnation pressure found in the wind tunnel test. In the computations, the Mach number of the test run is specified together with the static pressure and temperature from the experiment. The dynamic viscosity of nitrogen is determined by Sutherland's law [22] with the parameters given in Tab. 1.

2.3 Finite Element Model

Figure 2 shows the CAD assembly of the NLF-ECOWING-FSW as it is used in the finite element (FE) analysis. The FE model consists of the main wing in its jig shape, the wing adapter, and the cover plate on the lower surface of the wing. The adapter connects the wing with the wind tunnel support and the fuselage. The cover plate allows access to two compartments, which are necessary to integrate measurement equipment into the wing. Smaller details like pressure sensor ducts are disregarded to reduce the overall model complexity.
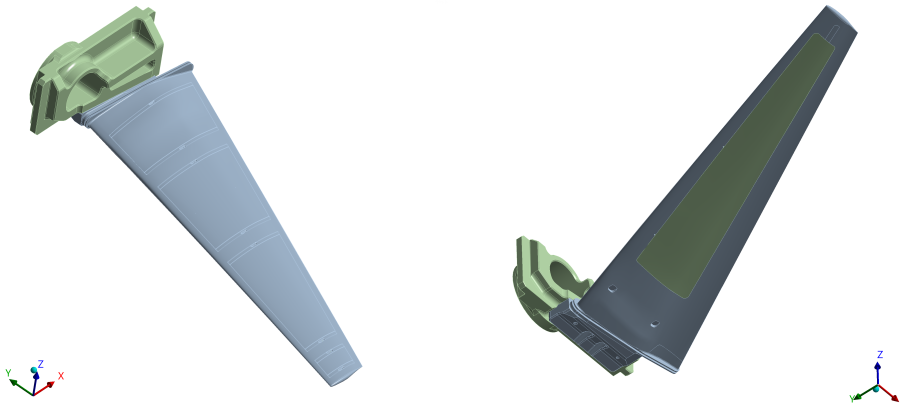
Figure 2: CAD assembly used to build the finite element model.

ANSYS® Mechanical Enterprise, Release 2022 R2 [23] is used to set up the model and perform the modal analysis. The FE model consists of $292\,757$ elements ($514\,389$ nodes). The modal description of the first six modes is used in the steady and unsteady CFD-CSM coupling. A structural test is performed with the wind tunnel model mounted in the test section using the integrated accelerometers. The experimental and numerical eigenfrequencies are given in Tab. 2. The experimental set-up only allows the identification of out-of-plane modes.

Table 2: Experimental and numerical mode shapes.

no.	description	num. frequency	exp. frequency	err.
1	1st bending	$30.38\,\mathrm{Hz}$	$29.0\,\mathrm{Hz}$	$+4.76\,\%$
2	2nd bending	$105.85\,\mathrm{Hz}$	$99.0\,\mathrm{Hz}$	$+6.92\,\%$
3	1st in-plane	$176.27\,\mathrm{Hz}$		
4	3rd bending	$232.11\,\mathrm{Hz}$		
5	1st torsion	$274.79\,\mathrm{Hz}$	$283.7\,\mathrm{Hz}$	$-3.14\,\%$
6	4th bending	$384.28\,\mathrm{Hz}$		

2.4 Grid Generation

Centaur™ V16.0 by CentaurSoft [24] is used to build CFD grids for the design and jig shape. The hybrid grids consist of a structured quadrilateral surface mesh on the wing with 300 grid points in chord and spanwise direction. An unstructured triangular mesh is used on the wing tip and fuselage, and an unstructured quadrilateral surface mesh on the belly fairing. Hexahedral and prismatic cells with nominally 75 layers are created upon the respective quadrilateral and triangular surface meshes on the wing. On the fuselage and belly fairing a nominal value of 85 layer is used. The first layer height is approximately $1.84 \cdot 10^{-7}\,\mathrm{m}$ with a growth rate of 1.1. The first cell height results in $y_{1,\,\mathrm{max}}^{+} < 1$ for all computations presented. The overall mesh consists of approximately $19.5 \cdot 10^{6}$ grid point.

3 RESULTS

3.1 Steady Results

Figure 3 shows the full angle of attack range measured in the experiment at $M = 0.78$ and $Re = 16 \cdot 10^6$. Computations are performed in this range for the rigid jig and flight shape with free boundary layer transition on the upper wing surface. The boundary layer flow on the fuselage is tripped close to the nose and the flow on the lower surface is tripped at the local $5\,\%$ chord position in the experiment and the CFD computations. The computations agree well with the experimental data in the range $-1° \le \alpha \le 2°$. For these angles of attack, transition occurs at the shock location. For lower angles of attack, crossflow transition is found, which is not considered in the current transition model set-up. At higher angles of attack, a strong separation at the wing-fuselage intersection on the upper surface is predicted by the CFD computations, which is not found in that extent in the experimental data.
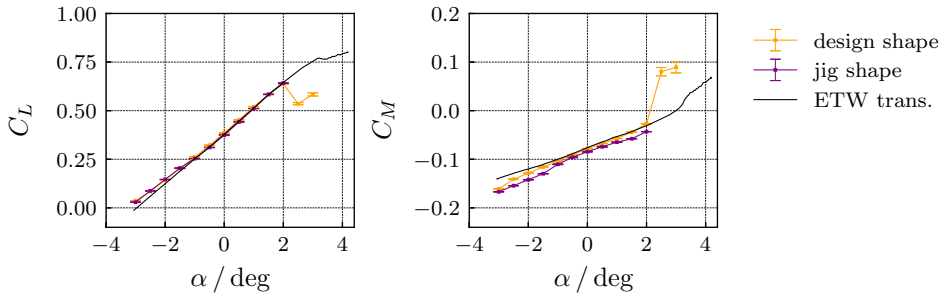
Figure 3: Transitional lift and moment coefficient curves in the full experimental angle of attack range.

Figure 4 shows the aerodynamic data close to the design lift coefficient of $C_L = 0.52$. In addition to the rigid computations, coupled CFD-CSM computations are shown. These include computations with free transition on the upper surface with and without turbulent wedges. The numerical disturbance locations at the wedge apices are based on the experimental temperature sensitive paint (TSP) measurements. The coupled computations without turbulent wedges overpredict the lift coefficient. Once turbulent wedges are included in the flow model, a good agreement is found for the lift coefficient and the prediction for the moment coefficient is improved as well.
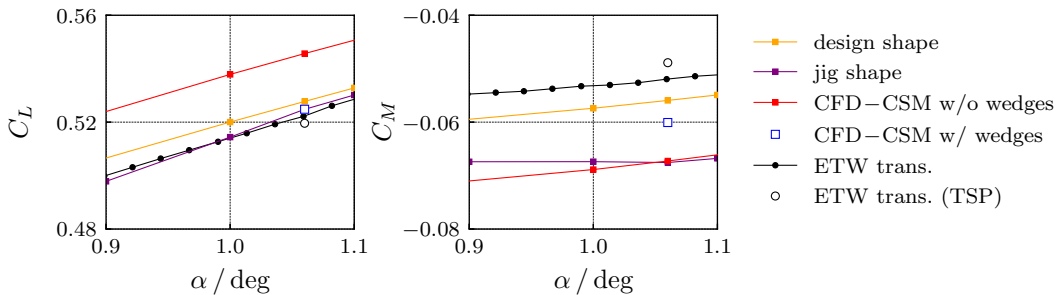

Figure 4: Experimental and computed lift and moment coefficient curves close to the design lift coefficient.

Figure 5 shows the experimental and computed bending and twist distribution with free transition with and without turbulent wedges at $\alpha = 1.06°$. As deformation and TSP measurements are not performed at the same time, deformation data for $\alpha = 1.082°$ is used for comparison. Both computational settings give a good representation of the model deformations. The deformations increase slightly for the flow without turbulent wedges as the aerodynamic loads are a

little higher due to the larger extent of laminar flow.
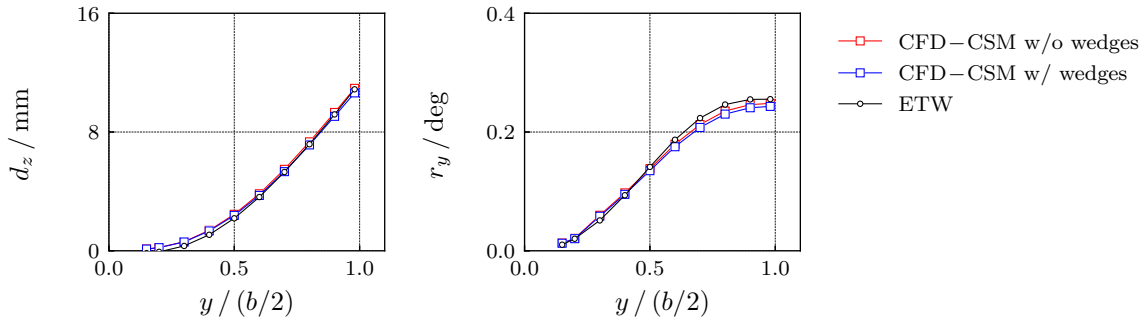

Figure 5: Bending and twist distribution for transitional flows with and without turbulent wedges.

Figure 6 shows the experimental TSP data [25] and the computed skin friction coefficient distributions on the upper surface of the wing. Four TSP measurement fields are integrated in the surface to detect the transition location. A temperature step method, heating based on carbon nanotubes, and heating through an infra-red laser technique are tested in the experiment to generate the temperature change to acquirer the TSP images [26]. The data in Fig. 6 are obtained by using the temperature step method.

The black dots between the TSP fields mark the locations of pressure sensors. Close to the fuselage, 62 static pressure ports are distributed on the upper and lower wing surface (row A). A total of 61 unsteady pressure transducers are located in three measurement rows (B to D) on the upper surface. The pressure transducers are staggered to avoid measurements in turbulent flow emerging from upstream located sensors.
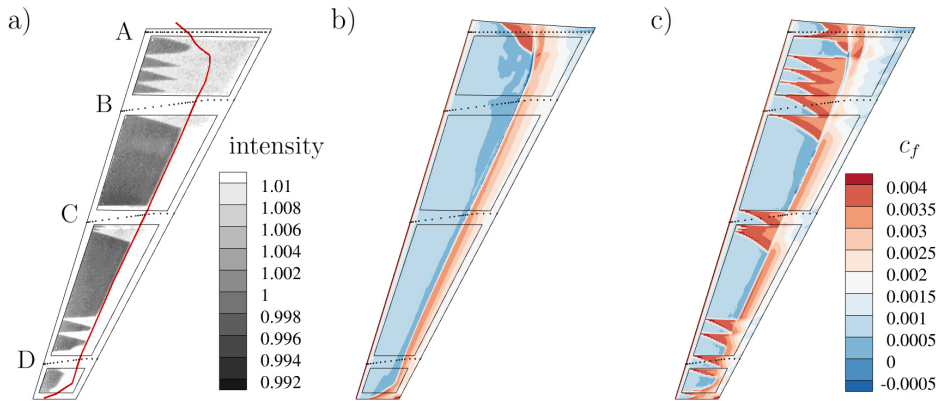

Figure 6: a) TSP light emission intensity with transition location from CFD-CSM computation, b) computed c_f distribution for free transition, c) computed c_f distribution with turbulent wedges.

Figure 6 a) shows the measured TSP light emission intensity at $\alpha = 1.06°$. The transition location and turbulent wedges are found where the light emission increases. The computed transition location from the CFD-CSM computation with free transition (Fig. 6 b) is included as a red line. The DLR γ transition model gives a good prediction of the transition location except for the most outer TSP pocket. Figure 6 c) shows the coupled CFD-CSM computation with turbulent wedges. The wedge angles are slightly larger than in the experiment and the orientation of the angle bisectors is too steep towards the leading edge.
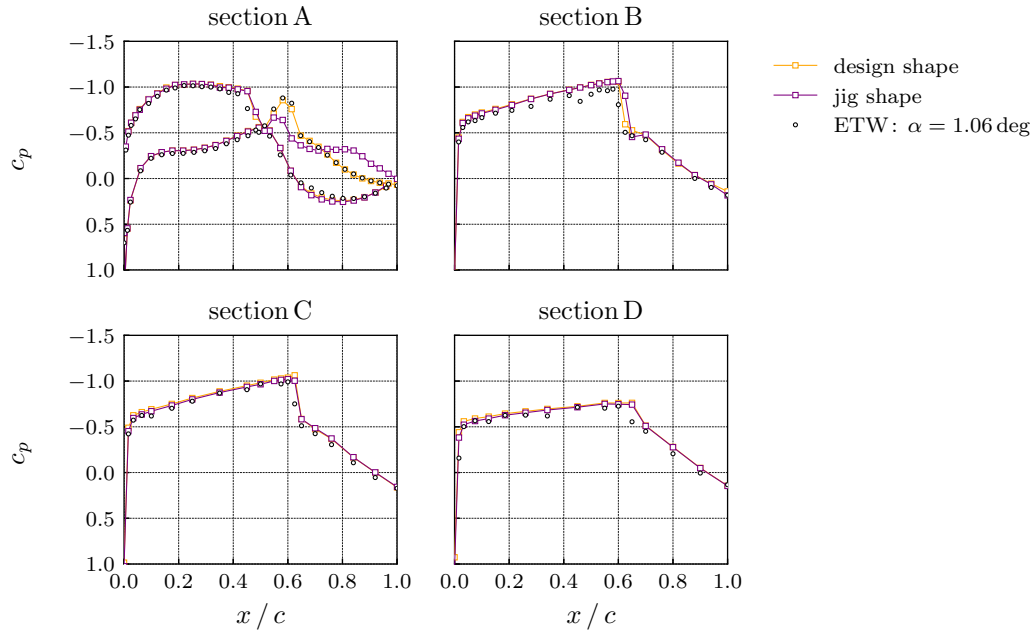
Figure 7: Pressure coefficient distributions evaluated at the experimental pressure orifice locations for the rigid jig and design shape computations with free transition at $\alpha = 1.06°$.
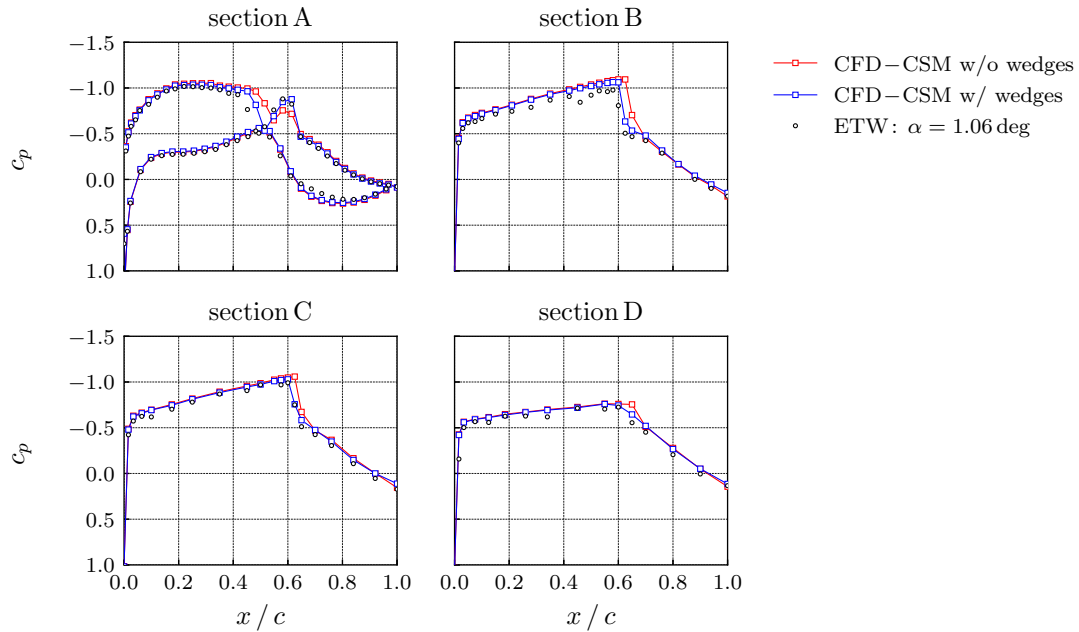

Figure 8: Pressure coefficient distributions evaluated at the experimental pressure orifice locations for the CFD-CSM computations with and without turbulent wedges at $\alpha = 1.06°$.

Figure 7 and 8 show the measured and computed pressure coefficient distributions for the rigid jig and design shape with free transition and the CFD-CSM results with and without turbulent wedges at $\alpha = 1.06°$, respectively. The main difference between design and jig shape is found for section A, where the double shock system and the downstream pressure recovery found in the experiment are not reproduced for the rigid jig shape. The coupled computation without turbulent wedges gives a shock position too far downstream in all measurement sections. The results for all sections are improved by the turbulent wedge model.

3.2 Unsteady Results

Following the first wind tunnel performance test, the NLF-ECOWING-FSW wing is tested in unsteady flow with a pitch excitation about its quarter chord line in a second wind tunnel campaign. As a preliminary investigation, the set-up presented in this investigation is used to perform a study on the unsteady aerodynamics of the wing with free boundary layer transition. In addition, the effect of turbulent wedges on the computational results is assessed. It should be noted that the wing in the unsteady experiment is decoupled from the fuselage to allow a pitch motion of the wing alone. The system will therefore show a different structural behavior as it is then connected to the drive shaft of the pitch oscillator.

A linearized pitch mode about the wing's quarter-chord line is defined and used for the sinusoidal excitation of the wing in the coupled CFD-CSM computation. The computations are performed at the test point described above at a mean angle of attack of $\alpha = 1.06°$ starting at the deformed state of the wing. A pitch amplitude of $\hat{\alpha} = 1°$ at different reduced frequencies $k = (c/2)\,\omega/U_\infty$ is investigated. The same time step size of $\Delta t = 10^{-4}$ sec is used in each computation. The computations are performed with free boundary layer transition on the upper surface without any turbulent wedges, with turbulent wedges as detected in the wind tunnel experiment for $\alpha = 1.06°$, and for a fully turbulent flow. In addition, computations for a rigid wing are performed with free transition and turbulent wedges.
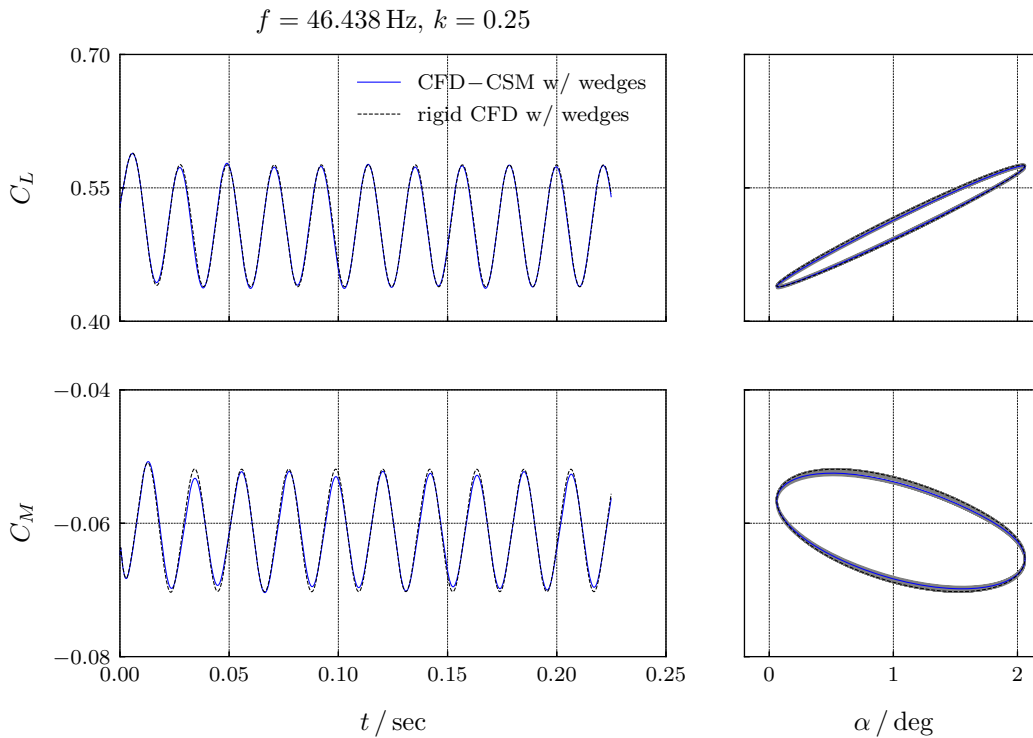

Figure 9: Lift and moment coefficient over time and phase averaged coefficients over angle of attack at $k = 0.25$ for the coupled and rigid system. Additionally to the phase averaged data, the last five periods are shown.

Figure 9 shows the variation of the lift and moment coefficient over time for a reduced frequency of $k = 0.25$ for the coupled and rigid system with free transition and turbulent wedges. The flexibility of the structure results in a more complex response as the structural modes are excited as well. For both settings, there is a deviation of the mean lift and moment coefficient from the initial stationary condition. This behavior is found for the fully turbulent, transitional flow with and without turbulent wedges, and for the rigid system as well. The deviation increases with

reduced frequency and it is not affected by the time step size. On the right side of Fig. 9, the phase averaged coefficients are shown together with the last five periods (gray), for which the averaging is performed.

Figure 10 shows the instantaneous skin friction coefficient distributions during a pitch period at $k = 0.25$ for free boundary layer transition with turbulent wedges. The turbulent wedges are preserved over the whole pitch period as intended. Between the turbulent wedges, there is no significant change in the transition position over the pitch period. Larger changes occur in the inboard wing section where the double shock system changes (local decrease in c_f) with periodically occurring boundary layer separation at the shock foot.

Based on the phase averaged lift $\overline{C}_L$ and moment $\overline{C}_M$ coefficients for each reduced frequency, the unsteady aerodynamic coefficients with respect to the pitch motion are defined:

$$\overline{C}_{L\alpha}(ik) = \frac{\text{FFT}\{\overline{C}_L(t)\}}{\text{FFT}\{\alpha(t)\}}, \tag{3}$$

$$\overline{C}_{M\alpha}(ik) = \frac{\text{FFT}\{\overline{C}_M(t)\}}{\text{FFT}\{\alpha(t)\}}. \tag{4}$$
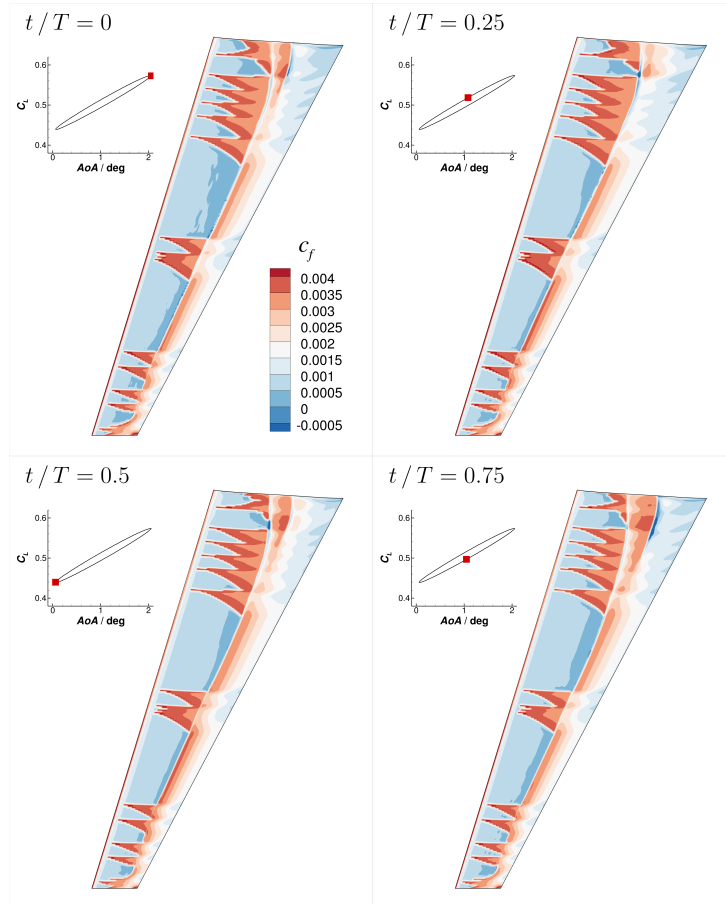

Figure 10: Instantaneous skin friction coefficient distributions during a pitch period at $k = 0.25$ for free boundary layer transition with turbulent wedges. The surface data are mapped onto the undeformed wing surface.
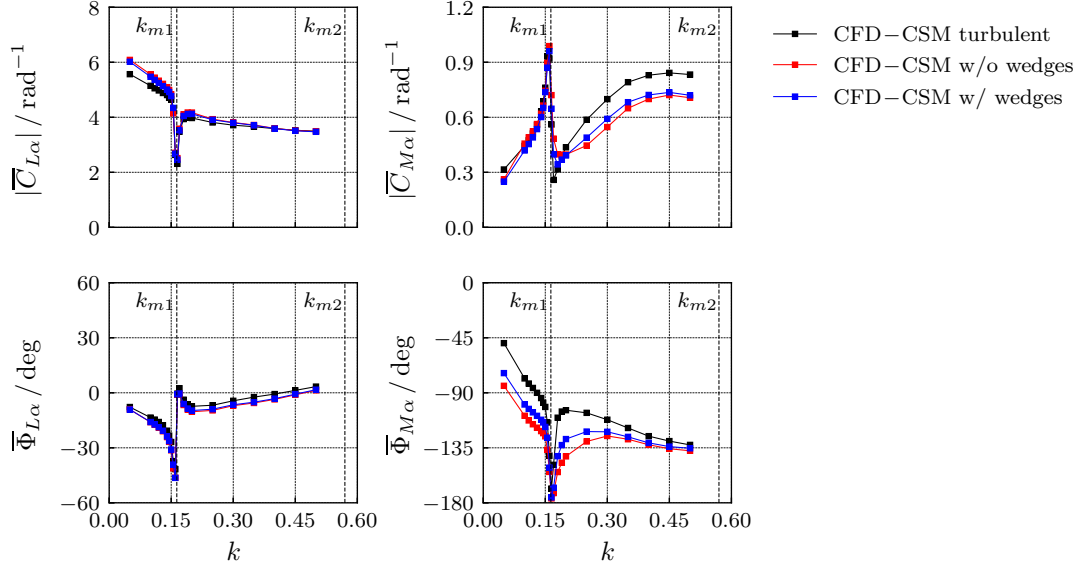
Figure 11: Unsteady lift and moment coefficients for a fully turbulent, a transitional flow without, and with turbulent wedges.
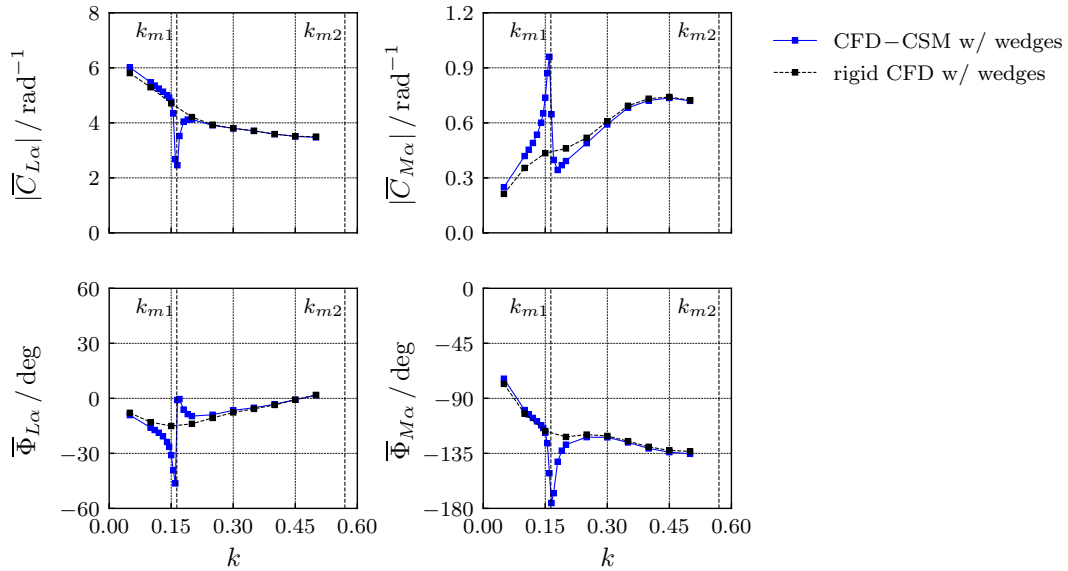

Figure 12: Unsteady lift and moment coefficients of the coupled and rigid wing in a transitional flow with turbulent wedges.

Figure 11 shows the unsteady lift and moment coefficients for a fully turbulent, a transitional flow without, and with turbulent wedges. Especially for the moment coefficient significant differences are found in magnitude and phase between the fully turbulent flow and both free transitional settings. The reduced structural eigenfrequencies k_{mi} are added as reference in Fig. 11. Once the excitation is close to the eigenfrequency of the first bending mode, a strong resonance occurs in the coupled CFD-CSM computations. The moment coefficient data for the transitional flow indicates a somewhat larger aerodynamic damping as the resonance peak gets slightly broader. For comparison, Fig. 12 shows the unsteady aerodynamics for the rigid pitching wing. No resonance is found as the eigenfrequencies are no longer excited.

4 CONCLUSION

This article presents steady and unsteady numerical computations for a wind tunnel test of a forward swept laminar wing configuration. A key goal of the wind tunnel test is to provide data for the validation of the intermittency-based DLR γ transition model in high Mach and Reynolds number flows. The computations show that the correlation-based transition model is capable to predict transition in the linear lift curve region correctly. In this angle of attack range, transition occurs at the shock location. Additionally, a method to introduce turbulent wedges in the laminar boundary layer flow is used to improve the agreement between computed results and experimental data further. Once turbulent wedges are included, a more precise prediction of the aerodynamic coefficients and the pressure distributions is possible.

As a precursor of an unsteady wind tunnel test, unsteady computations are performed to evaluate the unsteady aerodynamics of a pitching wing with free boundary layer transition. Overall significant differences between the fully turbulent and transitional flow are seen, stressing the importance of appropriate transition models for a valid aeroelastic assessment of future laminar aircraft configurations. The specific effect of the turbulent wedges is rather small compared to the steady observations.

Future investigations will address specific details, e.g. grid effects, number of structural modes, and time step size for the steady and unsteady computations. In addition, an assessment of measurement points in the full experimental angle of attack range will be performed. This includes crossflow transition cases at low angles of attack and more complicated flow conditions in the non-linear lift curve region at high angles of attack.

ACKNOWLEDGEMENT

5 REFERENCES

[1] Schulz, M. (2022). LuFo VI-2 ULTIMATE Forward-Swept Wing Half Model Performance Test in ETW. Test Report E 9018 TR 214, ETW.

[2] Seitz, A., Hübner, A., and Risse, K. (2020). The DLR TuLam project: design of a short and medium range transport aircraft with forward swept NLF wing. *CEAS Aeronautical Journal*, 11, 449–459. doi:10.1007/s13272-019-00421-1.

[3] Davies, K.-M., Fehrs, M., and Helm, S. (2022). Static aeroelasticity of a wind tunnel model with a forward-swept laminar wing. In: 19th International Forum on Aeroelasticity and Structural Dynamics, IFASD, IFASD-2022-168. Madrid, 13–17 June.

[4] Krumbein, A., Krimmelbein, N., and Schrauf, G. (2009). Automatic transition prediction in hybrid flow solver, part 1: Methodology and sensitivities. *Journal of Aircraft*, 46(4), 1176–1190. doi:10.2514/1.39736.

[5] Krumbein, A., Krimmelbein, N., and Schrauf, G. (2009). Automatic transition prediction in hybrid flow solver, part 2: Practical application. *Journal of Aircraft*, 46(4), 1191–1199. doi:10.2514/1.39738.

[6] Helm, S., Davies, K., and Fehrs, M. (2024). First comparison of cfd simulation and wind tunnel test of the forward-swept natural laminar flow model nlf-ecowing-fsw. In A. Dillmann, G. Heller, E. Krämer, C. Wagner, and J. Weiss (Eds.), *New Results in Numerical and Experimental Fluid Mechanics XIV*. Cham: Springer Nature Switzerland. ISBN 978-3-031-40482-5, pp. 425–434. doi:10.1007/978-3-031-40482-5_40.

[7] Helm, S., Fehrs, M., Kaiser, C., et al. (2023). Numerical simulation of the common research model with natural laminar flow. *Journal of Aircraft*, 60(2), 449–460. doi:10.2514/1.C036889.

[8] François, D. G., Krumbein, A., Krimmelbein, N., et al. (2023). Simplified stability-based transition transport modeling for unstructured computational fluid dynamics. *Journal of Aircraft*, 60(6), 1773–1784. doi:10.2514/1.C037163.

[9] Fehrs, M. and Helm, S. (2024). Turbulent wedge modeling in local correlation-based transition models. In A. Dillmann, G. Heller, E. Krämer, C. Wagner, and J. Weiss (Eds.), *New Results in Numerical and Experimental Fluid Mechanics XIV*. Cham: Springer Nature Switzerland. ISBN 978-3-031-40482-5, pp. 415–424. doi:10.1007/978-3-031-40482-5_39.

[10] Schwamborn, D., Gerhold, T., and Heinrich, R. (2006). The DLR TAU-Code: Recent applications in research and industry. In *ECCOMAS 2006*. Delft.

[11] Menter, F. R., Kuntz, M., and Langtry, R. (2003). Ten years of industrial experience with the sst turbulence model. In K. Hanjalić, Y. Nagano, and M. Tummers (Eds.), *Turbulence, Heat and Mass Transfer 4*. Redding: Begell House, Inc., pp. 625–632.

[12] Spalart, P. (2000). Strategies for turbulence modelling and simulations. *International Journal of Heat and Fluid Flow*, 21(3), 252–263. ISSN 0142-727X. doi:https://doi.org/10.1016/S0142-727X(00)00007-2.

[13] Smirnov, P. E. and Menter, F. R. (2008). Sensitization of the sst turbulence model to rotation and curvature by applying the spalart-shur correction term. vol. 6: Turbomachinery, Parts A, B, and C of *Turbo Expo: Power for Land, Sea, and Air*. pp. 2305–2314. doi:10.1115/GT2008-50480.

[14] Swanson, R. C. and Turkel, E. (1992). On central-difference and upwind schemes. *Journal of Computational Physics*, 101(2), 292–306. doi:10.1016/0021-9991(92)90007-L.

[15] Dwight, R. (2006). *Efficiency Improvements of RANS-Based Analysis and Optimization using Implicit and Adjoint Methods on Unstructured Grids*. Ph.D. thesis, University of Manchester, Manchester.

[16] Jameson, A. (1991). Time dependent calculations using multigrid, with applications to unsteady flows past airfoils and wings. In 10th *Computational Fluid Dynamics Conference*, AIAA 91-1596. Honolulu: AIAA. doi:10.2514/6.1991-1596.

[17] Reimer, L. (2015). The flowsimulator – A software framework for cfd-related multidisciplinary simulations. In: European NAFEMS Conference: Computational Fluid Dynamics (CFD) – Beyond the Solve. München, 2–3 December.

[18] Broyden, C. G. (1965). A class of methods for solving nonlinear simultaneous equations. *Mathematics of Computation*, 19(92), 577–593. ISSN 00255718, 10886842. doi:10.2307/2003941.

[19] Duchon, J. (1977). Splines minimizing rotation-invariant semi-norms in sobolev spaces. In W. Schempp and K. Zeller (Eds.), *Constructive Theory of Functions of Several Variables*. Berlin: Springer. ISBN 978-3-540-37496-1, pp. 85–100. doi:10.1007/BFb0086566.

[20] Barnewitz, H. and Stickan, B. (2013). Improved mesh deformation. In B. Eisfeld, H. Barnewitz, W. Fritz, and F. Thiele (Eds.), *Management and Minimisation of Uncertainties and Errors in Numerical Aerodynamics: Results of the German collaborative project MUNA*. Berlin: Springer. ISBN 978-3-642-36185-2, pp. 219–243. doi:10.1007/978-3-642-36185-2_9.

[21] Newmark, N. M. (1959). A method of computation for structural dynamics. *Journal of Engineering Mechanics*, 85(EM3), 67–94.

[22] White, F. (2006). *Viscous Fluid Flow*. New York: McGraw-Hill, 3 ed.

[23] Ansys® Mechanical Enterprise (2022). Mechanical user's guide, release 2022 r2. ANSYS, Inc., Canonsburg.

[24] CentaurSoft (2023). CENTAUR grid generator. `https://www.centaursoft.com`. Accessed: 2023-10-24.

[25] Van Hinsberg, N., Henne, U., Weiss, A., et al. (2023). Temperature sensitive paint measurement in ETW for investigation of the natural laminar flow on an innovative forward swept wing. In *Dt. Luft- und Raumfahrt Kongress, DLRK*. Stuttgart.

[26] Klein, C., Henne, U., Deisuke, Y., et al. (2017). Application of carbon nanotubes and temperature sensitive paint for the detection of boundary layer transition under cryogenic conditions (invited). In *55th AIAA Aerospace Sciences Meeting*, AIAA 2017-0336. Grapevine: AIAA. doi:10.2514/6.2017-0336.

COPYRIGHT STATEMENT